Unraveling influential factors of stainless-steel dissolution in high-energy 1 lithium ion batteries with LiFSI-based electrolytes 2 Marian Cristian Stan¹, Peng Yan¹, Gerrit Michael Overhoff¹, Nick Fehlings², Hyung-Tae 3 4 Kim³, Robert Tobias Hinz¹, Tjark Thorben Klaus Ingber², Rayan Guerdelli¹, Christian Wölke¹, Martin Winter^{1,2}, Gunther Brunklaus¹ and Isidora Cekic-Laskovic^{1*} 5 6 7 ¹Institute of Energy Materials and Devices, Helmholtz Institute Münster: Ionics in Energy Storage 8 (IMD-4 / HI MS), Forschungszentrum Jülich GmbH, Corrensstraße 48, 48149 Münster, Germany 9 ²MEET Battery Research Center, University of Münster, Corrensstraße 46, 48149 Münster, Germany 10 ³LG Energy Solution, R&D campus Daejeon, 188 Munji-ro, Yuseong-gu, Daejeon 34122, Korea 11 12 *Corresponding Author: i.cekic-laskovic@fz-juelich.de; m.stan@fz-juelich.de 13 14 Abstract 15 16 Leveraging physicochemical advantages over lithium hexafluorophosphate (LiPF₆), lithium 17 bis(fluorosulfonyl)imide (LiFSI) is being investigated as a conducting salt for lithium 18 manganese-rich cathodes (LMR) and micro-crystalline silicon anodes (μ-Si). Nevertheless, its 19 behavior towards the aluminum (Al) current collector and stainless-steel (SUS) coin cell parts 20 limits its application under operating conditions requiring potentials higher than 3.9 V vs. Li|Li⁺. 21 Using a mixture of organic carbonate-based solvents, various functional additives, and LiPF₆ 22 lithium salt concentrations up to 1.0 M, the instability issue of the Al current collector in the 23 presence of LiFSI is avoided. However, stainless-steel dissolution remains, being confirmed by 24 both potentiodynamic measurements and SEM morphology investigations of the coin cell 25 components after linear sweep voltammetry measurements carried out to 5.0 V. The results also 26 indicate that the amount of stainless-steel dissolution is influenced by both the LiFSI amount 27 in the electrolyte and the quality (grade) of stainless-steel used. Using Al-coated SUS 316L 28 coin cell parts and/or high concentration electrolytes (HCE) with LiFSI (≈ 4 M LiFSI), the 29 observed stainless-steel dissolution process can be fully avoided, allowing the evaluation of the electrochemical performance of LMR cathodes with μ-Si anodes in LiFSI-based electrolytes. 30 31 32 Keywords: blended salt, LiFSI, stainless-steel dissolution, passivation, cycle performance 33

34

1. Introduction

1

2 The increasing demand for lithium ion batteries (LIBs), driven primarily by the expanding 3 electric vehicle (EV) market and the growing need for energy storage solutions, requires also an improvement in terms of energy density of such battery systems. [1,2] Research and 4 development efforts have been mainly focused on improving the energy density, safety, and 5 cycle life of LIBs at an affordable cost. [3] Innovations such as solid-state batteries and novel 6 7 electrode materials have been explored while the development of novel concepts and 8 components for high-performance electrolytes in high-voltage energy systems is also necessary.[4,5] 9 Currently, there are various tools available to support this development, ranging from 10 11 computational rationalization and artificial intelligence suggestions to experimental synthesis of new electrolyte components.^[6-9] Integrating the characteristic properties of various 12 13 components into novel electrolyte formulations is often used to develop high-performance electrolyte systems. [10,11] However, independent of the composition of such high-performance 14 15 electrolyte system formulations, a pivotal role of the electrolyte that is less regarded concerns 16 its induced instability towards the active/inactive materials of the LIB cells upon storage and operation.[12] 17 18 In case of lithium metal anodes (LMAs), unwanted side reactions upon contact with the 19 electrolyte, result in active material loss and a deterioration of electrochemical performance 20 even before charge transfer takes place. Along with the well-known electrolyte decomposition 21 process and the formation of the solid electrolyte interphase (SEI), two further processes 22 meaningfully impact the stability of LMAs. Kolesnikov and co-workers, along with Dohmann 23 and co-workers, have described the existence of a galvanic corrosion process that occurs when a Li|M galvanic couple (where M = Cu, Ni, stainless-steel) is exposed to liquid electrolyte. [13,14] 24 25 During this process, the difference in the standard potentials of the two metals results in a 26 dissolution of the LMA via lithium oxidation coupled with electrolyte decomposition on the M 27 surface. Lin and co-workers identified a Kirkendall-effect resulting in void formation on the 28 side of the Li|Cu electrode couple where the most diffusing species are present due to the interdiffusion between the two metals.^[15] Nevertheless, this effect is not particularly pronounced, 29 30 when the electrode couple is in contact with the electrolyte, but also occurs in the absence of 31 the electrolyte. Regardless of the electrolyte chemistry, both chemical corrosion with SEI 32 formation and galvanic corrosion coexist and can occur at the same time, yet, at different rates.[16] Kwon and co-workers indicated that the SEI at the LMA surface formed through 33 34 chemical corrosion of lithium bis(fluorosulfonyl)imide (LiFSI)-based electrolytes is of crucial

importance for suppressing the galvanic corrosion behavior. [17] Electrolytes with imide-based 1 2 lithium conducting salts (i.e. lithium bis(trifluoromethanesulfonyl)imide (LiTFSI) and LiFSI) also cause anodic dissolution of the aluminum (Al) current collector, which significantly 3 reduces the electrochemical performance of any LIB system. [18,19] Such behavior originates 4 5 from the high solubility of the reaction products formed between the TFSI and FSI and 6 the Al-substrate at high potentials, resulting in the formation of pitting and mechanical degradation of the current collector. [20,21] Therefore, strategies to counteract this process are 7 8 mainly based on the use of electrolyte additives resulting in the formation of a protective layer 9 on the aluminum surface, use of solvents/co-solvents with a lower dielectric constant than ethylene carbonate (EC), and engineering electrolytes or protective coatings.^[22–28] 10 11 While the above-mentioned processes are generally related to the electrolyte formulation and 12 the presence of imide-based lithium conducting salts, a particular side reaction that is mainly 13 characteristic to LiFSI is represented by the stainless-steel (SUS) instability at potentials higher 14 than 3.9 V vs. Li|Li⁺. When exposed to LiFSI based electrolytes above 3.9 V, stainless-steel can 15 undergo a dissolution process that compromises both the integrity of the inactive material and the performance of the resulting electrochemical system. [29] Stainless-steel is a ubiquitous 16 17 material known for its exceptional corrosion resistance and wide-ranging applications in various industries.^[30] In energy storage and conversion applications, stainless-steel is mainly 18 19 used for the inactive parts of various cell designs with only a few scientific reports on its use as 20 an active electrochemical material. In the latter, by creating a chromium-rich oxide (Cr₂O₃) 21 layer on the surface of the SUS current collector, an enhancement of the electrochemical performances compared to the synthesized powder active material was obtained. [31,32] Although 22 23 stainless-steel is generally considered a corrosion-resistant material, the presence of chloride 24 ions (Cl⁻) as impurities in LiFSI salts can cause passivation breakdown in stainless-steel by 25 penetrating the native oxide surface layer and reaching the metal surface, ultimately leading to metal dissolution.[33] 26 27 The mechanism leading to the stainless-steel dissolution and pit formation is quite complex 28 keeping in mind the complexity of the electrolyte formulations and the variable purity of the 29 imide-based salts. In several reports the authors described the reaction mechanism of stainless-30 steel dissolution in imide-based electrolytes. For that, Luo and co-workers suggested a 31 mechanism of stainless-steel dissolution involving three steps, where the electrolyte decomposition resulted in the formation of LiSO₃F. [33] In a following step, the attack of Cl⁻ and 32 SO₃F⁻ ions against the stainless-steel surface results in Fe²⁺ dissolution, oxidation to Fe³⁺ and 33 leaching into the electrolyte. [33] In the last step, the precipitation of Fe₂O₃ on the stainless-steel 34

1 surface is unable to fully re-passivate the surface, due to the poor adherence of the black deposit 2 (Fe₂O₃).^[12,33,34] It is very likely that the presence of Cl⁻ impurities in the LiFSI salts play an even more important role in SUS degradation, considering the high oxidative stability of the 3 FSI-anion. [35,36] As shown by Han and co-workers, the use of ultra-pure LiFSI (Cl 4 5 content < 1 ppm) in organic carbonate-based electrolytes inhibits any Al dissolution when the 6 potential was scanned to 5 V vs. Li|Li⁺. Consequently, LiCoO₂||C₆ cells with CR2032 coin-type 7 SUS parts showed good performance up to 4.2 V for more than 50 cycles.^[37] Based on these 8 reports, in LiFSI-based electrolytes, the presence of Cl⁻ impurities can have a significant role in 9 the stainless-steel dissolution and pit formation. Three mechanisms were postulated for the 10 breakdown of the passivation/oxide film by Cl⁻-ions: (1) a penetration mechanism involving 11 migration of the aggressive anions through the oxide film to the metalloxide interface; (2) an 12 adsorption mechanism resulting in the local Cl⁻ adsorption at the oxide surface leading to 13 increased dissolution; (3) a film breaking mechanism referring to the mechanical breakdown of 14 the oxide layer exposing small parts of the bare metal to the electrolyte, thus preventing the surface re-passivation. [38] Although the stability of the passivation film is mainly related to 15 16 stainless-steel alloy composition, other factors that influence the passivation film are 17 represented by the concentration of the aggressive anions in the electrolyte, potential, pH and temperature.[39,40] 18 19 Solutions oriented towards overcoming the stainless-steel dissolution considered the use of 20 other cell formats; e.g. pouch-cell format where the contact between the electrolyte and the 21 stainless-steel is avoided, use of Al-coated SUS coin cells parts, or employing other coatings for stainless-steel in order to reduce its susceptibility to chemical corrosion at the positive 22 23 electrode. [34,41,42] However, different researchers pointed out that both Al dissolution and stainless-steel dissolution side reactions can coexist in Al-clad SUS coin cell casings, making 24 25 interpretation of results quite difficult. [41,43] Engineered electrolytes using dual-salts or salt 26 blend concepts are used to combine, in a synergistic manner, the advantages that the single salts have in order to maximize the performance of certain lithium ion chemistries. [41,44] 27 Understanding the mechanisms behind stainless-steel dissolution in LiFSI-based electrolytes is 28 29 crucial for the development of more stable and reliable energy storage technologies realizing 30 the full potential of these electrolytes in practical applications. Therefore, the effect of various 31 grades of stainless-steel on the electrochemical performance needs to be investigated in LIBs similar to reports regarding other energy storage and conversion systems. [40,45–47] In this study, 32 33 using a potentiodynamic measurement under constant temperature conditions, the effect of the 34 pitting potential was investigated for electrolyte formulations containing various LiFSI

concentrations and with SUS 316 and SUS 316L coin cell parts. While the stainless-steel corrosion process with LiFSI is not a new phenomenon, we show that stainless-steel surface polishing and its compositions play a crucial role in understanding such behavior. The obtained results indicate that the kinetics of stainless-steel dissolution are affected by the LiFSI content in the electrolyte and the stainless-steel grade. Qualitative measurements of the surface coverage indicated a larger amount of dissolution pits for SUS 316 (0.08% carbon) substrate compared to SUS 316L (0.03%) analogues. The lower carbon content helps to minimize the risk of sensitization, which can lead to inter-granular corrosion in certain environments. Furthermore, we examine potential strategies for enhancing the compatibility of stainless-steel with LiFSI-based electrolytes, employing HCEs in full cell setup assembled with coin cell parts made of SUS 316 and SUS 316L, without any Al-coating. On the other side, using Al-coated SUS 316L coin cell parts, the electrochemical performance of cells containing a lithium manganese-rich cathode (LMR, Li_{1.34}Ni_{0.35}Mn_{0.65}O₂) cathode combined with micro-crystalline silicon (μ-Si) anode in LiFSI-based electrolytes were successfully investigated. These results offer valuable insights into the challenges and opportunities associated with the utilization of stainless-steel components in high-voltage LIBs technologies.

2. Results and discussion

19 2.1. Potentiodynamic anodic polarization

Potentiodynamic anodic polarization experiments (**Figure 1**) were carried out to 5 V in order to investigate the stability of SUS 316 and SUS 316L polished spacers in electrolyte formulations containing various amounts of LiFSI (**Table S1**). In **Figure S1** the schematic representation of the coin cell configuration used for this study is exemplified, indicating that only the 1 mm spacer and the casing at the positive side were changed. Figure 1a indicates that in the 0.6 M LiPF₆ + 0.6 M LiFSI in Gen 0 (EC:EMC 3:7 Vol. with 3 wt.% FEC, 1 wt.% VC, 1 wt.% DTD, 0.5 wt.% LiBF₄ and 0.5 wt.% PS) electrolyte, the substrate material composition impacts both the intensity of the oxidation current at 5 V as well as on the onset voltage of the oxidation process. A higher oxidation current is observed for SUS 316 spacer as compared to SUS 316L, while using an Al spacer results in a low oxidation current (equivalent to a current density of 6·10⁻³ mA cm⁻²). During these investigations, the contribution from the oxidative electrolyte decomposition cannot be ruled out. However, due to the low current observed on the Al working electrode, the contribution of electrolyte decomposition to the final value of the oxidation current is neglected. Although SUS 316L seems to have increased resistance towards the stainless-steel dissolution as compared to SUS 316, the amount of current evolved at 5 V

indicates that its passivity is also broken down. This continuous current increase during the potential scan indicates that the oxide layer gets broken, resulting in material dissolution. Furthermore, the effect of the stainless-steel dissolution current as a function of the scan rate is presented in Figure 1b. In contrary to the common behavior of a redox system where the oxidation current is proportional to the square root of the scan rate, a higher oxidation current is observed at lower scan rates. This suggests that the rate of stainless-steel dissolution process is kinetically hindered by the use of fast scan rates, where lower scan rates allow a longer time for the side reaction to proceed.

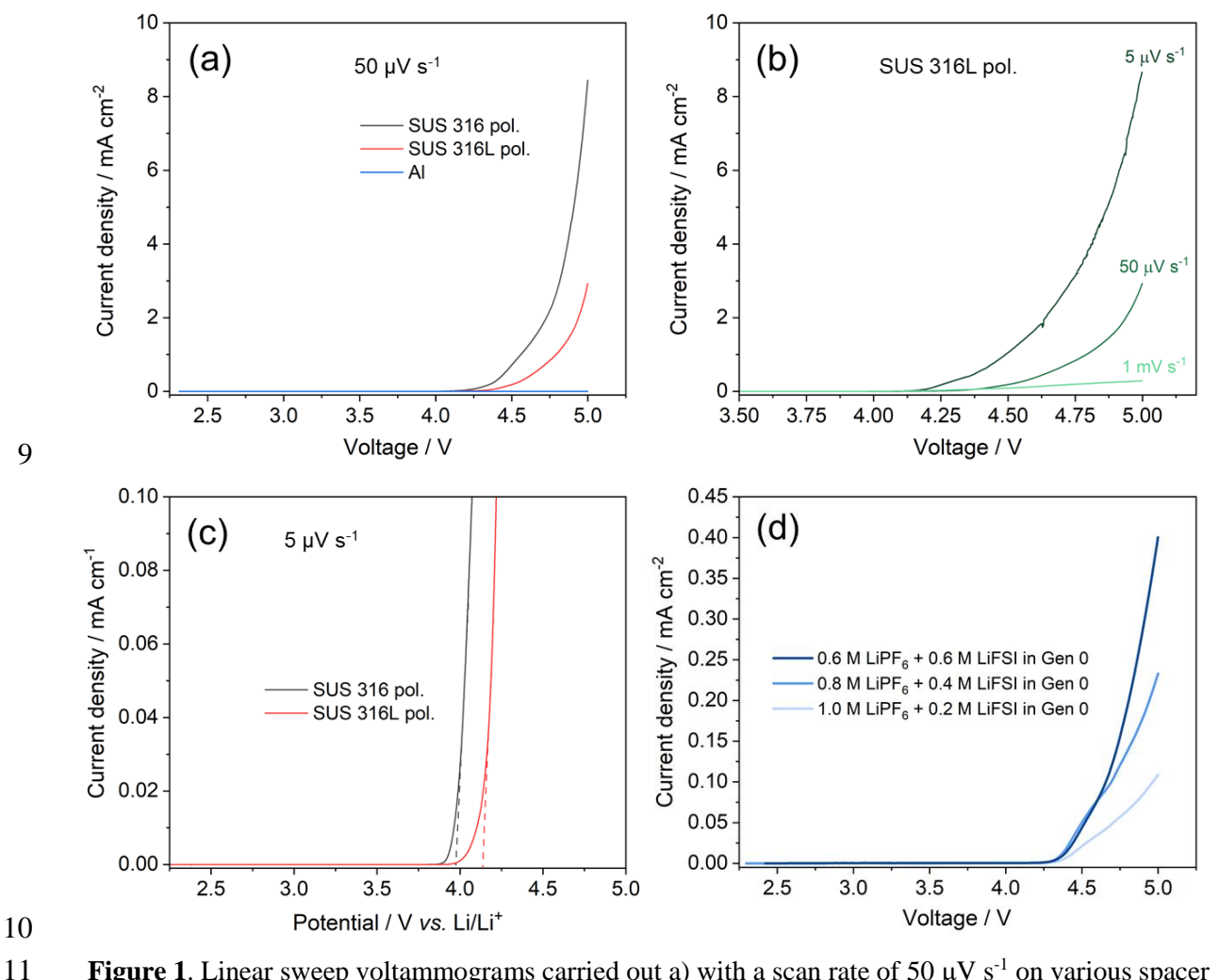


Figure 1. Linear sweep voltammograms carried out a) with a scan rate of 50 μ V s⁻¹ on various spacer materials; b) on polished SUS 316L spacer with different scan rates; and c) with a scan rate of 5 μ V s⁻¹ on polished SUS 316 and polished SUS 316L spacers using the 0.6 M LiPF₆ + 0.6 M LiFSI in Gen 0 as electrolyte. d) Effect of the LiFSI-content in Gen 0 on the current density with a scan rate of 250 μ V s⁻¹.

Pitting corrosion occurs above a certain potential also known as pitting potential that represents a measure of the instability of a metal in a certain medium. Using a 3-electrode CR 2032-coin cell set-up, with Li metal as counter electrode (CE) and reference electrode (RE), the potential of SUS 316 and SUS 316L was swept from OCP value to 5 V vs. Li|Li⁺ using a scan rate of 5 μ V/s (18 mV/h). The results in Figure 1c indicate a slight difference in the pitting potential

1 (intercept marked with dash line) of the two materials with the SUS 316L potential value 2 increased by 0.16 mV as compared to SUS 316 that showed 3.98 V vs. Li|Li⁺. As a "rule of 3 thumb", the higher the pitting potential, the higher is considered also the resistance of the 4 respective material against stainless-steel dissolution or corrosion. The value of the pitting 5 potential is dependent on various parameters, among which, surface quality (coating), 6 temperature, electrolyte composition and current density represent the most important ones. 7 The influence of LiFSI concentration on the evolved intensity of the oxidation current is 8 exemplified in Figure 1d using SUS 316L as working electrode while the overall ionic 9 conductivity of the formulated electrolytes by different temperatures is provided in **Figure S2** 10 and Table S1. In Figure 1d, a higher concentration of the LiFSI present in the electrolyte results 11 also in a higher intensity of the oxidation current when the voltage reaches 5 V. The extent of 12 stainless-steel dissolution indicates that the intensity of the oxidation current is largely affected 13 by the type of stainless-steel, LiFSI concentration and scan rate used.

14

15

16

17

18

19

20

21

22

23

24

25

26

27

28

29

30

31

32

33

34

2.2. Morphological evolution of stainless-steel spacers after LSV measurement

coin-cells, washed with ethyl methyl carbonate (EMC) several times, and dried under reduced pressure before the SEM images were recorded. The images of the stainless-steel surface morphology evolution after the LSV measurements are comparatively presented in **Figure 2**. Comparing the surface morphology of the SUS 316 spacers after the potential was scanned to 5 V at various scan rates, it is easily observable that the surface morphology is characterized by localized stainless-steel dissolution that led to the formation of pits. In Figure 2a-c the size of the steel-dissolution pits is decreasing with increasing scan rate. This confirms that the stainless-steel dissolution is a kinetically limited process, where the possible adsorption of the electrolyte species on the surface of the electrode is the limiting process. Furthermore, this implies that adsorption of the Cl⁻ and FSI⁻ anions still occurs even at high scan rates; however, the metal dissolution is probably hindered due to a possible re-passivation process that occurs faster than the stainless-steel dissolution process. In contrary, at a slower scan rate, although the surface of the stainless-steel is re-passivated, the attack of the Cl⁻ and FSl⁻ anions destabilizes this layer, resulting in an extended stainless-steel dissolution. A similar trend is also observed for the SUS 316L steel-grade as depicted in Figure 2d-f.

After the LSV measurements, SEM images of the stainless-steel spacers were collected in order

to visualize the effect of scan rate, electrolyte formulation and material composition on the

stainless-steel dissolution process. For that, the stainless-steel spacers were recovered from the

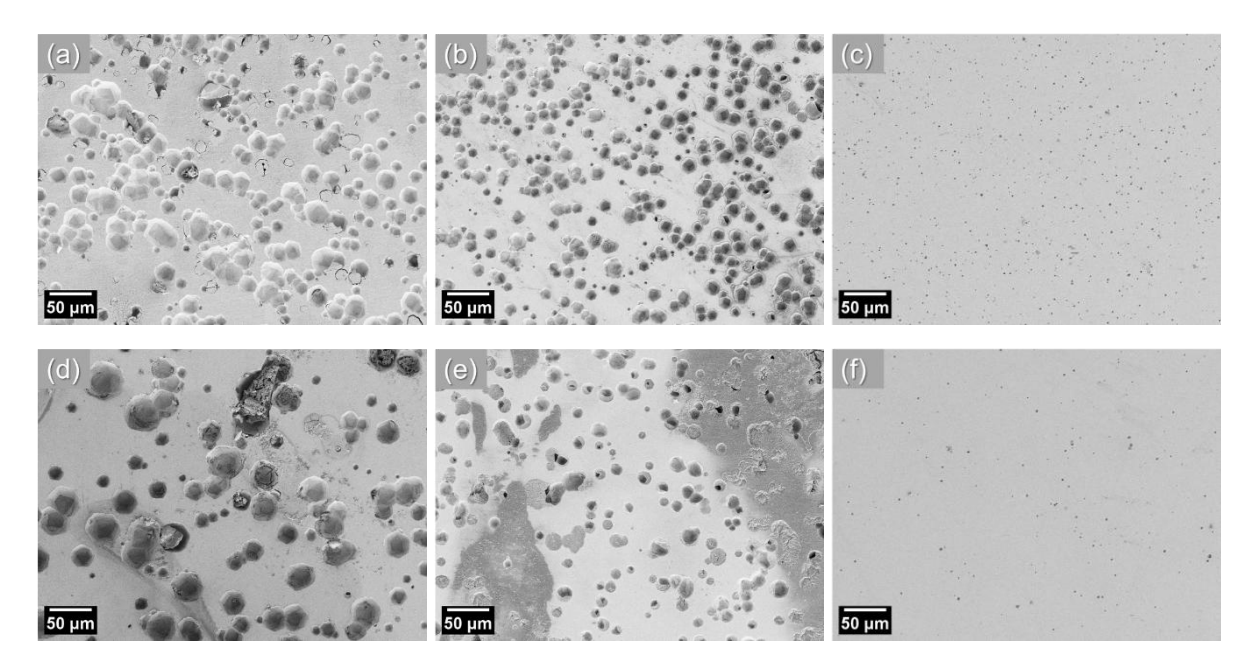


Figure 2. SEM images of a)-c) SUS 316 and d)-f) SUS 316L spacer after the linear sweep voltammetry measurements carried out to 5 V with a scan rate of a),d) 5 μ V s⁻¹, b),e) 50 μ V s⁻¹ and c),f) 1 mV s⁻¹ using the 0.6 M LiPF₆ + 0.6 M LiFSI in Gen 0 as electrolyte. All images were recorded with an acceleration voltage of 3 kV with WD of 5 mm, magnification of 250x and using SE detector.

The SEM images in Figure 2 further reveal noteworthy differences between the two stainless-steel grades, independent of the scan rate used. Such differences can be easily quantified for the two materials by measuring how much of the stainless-steel surface is covered with dissolution pits. While the size of the pits is hardly affected by the stainless-steel grade, the surface coverage is always lower for the SUS 316L steel. **Figure S3** shows the high magnification SEM images, representing the morphology of the SUS 316 and SUS 316L electrodes after LSV to 5 V in 2-electrode cells with a scan rate of 1 mV s⁻¹. Based on Figure S3 the surface coverage of the pits was calculated to be 2.02% for the SUS 316 electrode and 0.59% for SUS 316L, respectively. These results are also in accordance with the values observed for the oxidation current densities depicted in Figure 1, supporting a more serious stainless-steel dissolution in the case of the SUS 316 grade. **Figure S4** shows SEM images of the pitting corrosion that occurred on SUS 316L spacers with different amounts of LiFSI in the electrolyte. These images indicate that lower concentrations of LiFSI in the electrolyte result in fewer and shallower pits on the stainless-steel surface, reducing the surface coverage, compared to higher concentration electrolytes (e.g. 0.6 M LiPF₆ + 0.6 M LiFSI in Gen 0).

2.3. Morphological evolution of the μ -Si electrodes with SUS 316 coin-cell parts

The use of SUS 316 in coin cells with LiFSI based electrolytes was shown previously to depend primarily on the reactivity of certain electrolyte components with the stainless-steel surface. In

1 the case of LMR $\|\mu$ -Si cells with 0.6 M LiPF₆ + 0.6 M LiFSI in Gen 0 as electrolyte, the inability 2 to charge the positive active material above 4.2 V (during the time limited constant current step) 3 was already observed during the formation cycle as presented in Figure S5, independent on the 4 type of stainless-steel spacer used. Furthermore, during the constant voltage step at 4.65 V, a 5 large amount of current evolved due to side reactions. The cells could not be reversibly cycled 6 due to the stainless-steel dissolution process that predominated over the expected 7 electrochemical behavior of the LMR $\parallel \mu$ -Si cell chemistry. 8 *Post mortem* analysis of the μ -Si anode after the failed formation cycle of LMR $\parallel \mu$ -Si cells was 9 carried out by recording SEM images of the μ-Si electrode at two different positions: one close 10

to the edge and one close to the middle of the electrode. **Figure 3** shows the SEM images of the respective areas as well as an overlay of the element mapping. In Figure 3a and b the morphology of the μ-Si electrode indicates significant differences between the regions close to

morphology of the μ -SI electrode indicates significant differences between the regions close to

13 the edge and the middle of the μ -Si anode.

11

12

14

1516

17

18

19

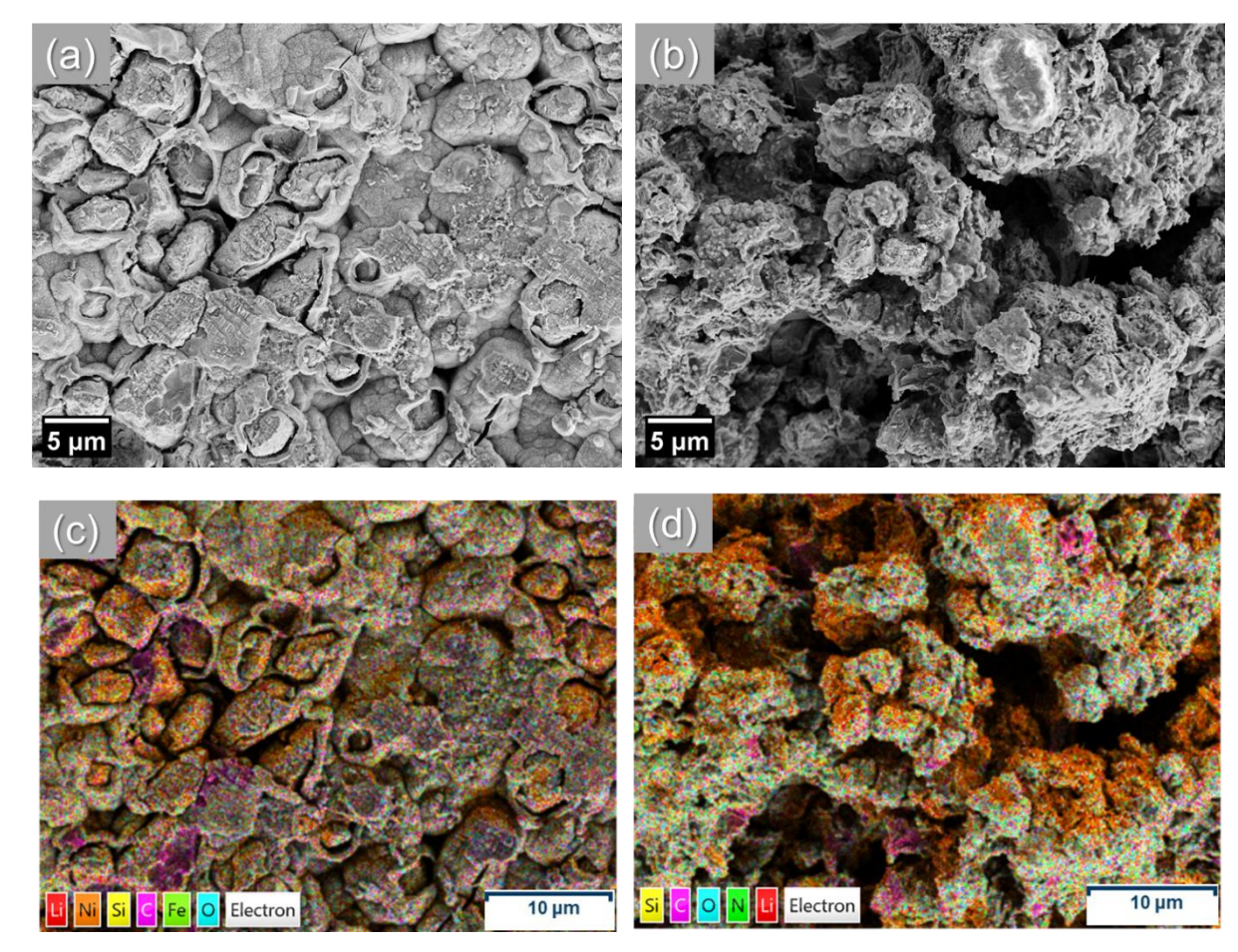


Figure 3. Post mortem SEM images of the μ -Si electrodes after the cell containing 0.6 M LiPF₆ + 0.6 M LiFSI in Gen 0 as electrolyte was kept at 4.65 V. The SEM images indicate an area a) near the edge and b) near the middle of the 15 mm diameter negative electrode. The corresponding EDX mapping of the respective areas is provided in c) and d).

- 1 Energy dispersive X-ray spectroscopy (EDX) mapping (Figure 3c and d) confirms that
- 2 stainless-steel dissolution products (i.e. Fe and Ni) are more prevalent in the regions adjacent
- 3 to the edge of the μ -Si electrode. In contrast, the areas in the middle of the electrode mainly
- 4 contain elements characteristic for electrolyte decomposition products (such as alkyl carbonates,
- 5 LiF, Li₂CO₃, SiOF, etc.).
- 6 Considering the difference in the size of the LMR-electrode (i.e. 14 mm diameter) and that of
- 7 the SUS 316 spacer (i.e. 15 mm diameter), when the cell is polarized to a voltage higher than
- 8 4.2 V, Fe dissolution occurs according to the mechanism proposed by Luo and co-workers.^[33]
- 9 Due to the lower potential of the μ -Si electrode, the dissolved Fe-species will be re-deposited
- at the surface of the negative electrode. The electrochemical activation of the LMR-cathode is
- interrupted by the excessive steel-dissolution process that negatively affects the performance
- and stability of the active materials, indicated by the cell's incapacity to reach voltages higher
- than 4.2 V. Using electrolyte formulations with less LiFSI (1.0 M LiPF₆ + 0.2 M LiFSI in Gen
- 14 0) and SUS 316L cell components, the stainless-steel dissolution was apparently overcome for
- several cycles, with the positive active material being able to be activated to 4.65 V. However,
- these cells were characterized by a fast capacity fading, most likely due to the stainless-steel
- 17 dissolution process surpassing the cathode material redox reactions and electrolyte
- decomposition (**Figure S6**).

- 20 2.4. Surface composition of SUS 316-type coin cells parts
- 21 The compatibility issues of LiFSI with SUS 316 stainless-steel mainly arise due to the presence
- of Cl⁻ ions that originate from impurities of the LiFSI salt, causing a deterioration of the native
- 23 oxide layer on the surface of stainless-steel. The resulting surface composition evolution of
- various pristine stainless-steel grades was investigated using X-ray photoelectron spectroscopy
- 25 (XPS) sputter depth profiling. The results are presented in **Figure 4**. The thickness of the native
- oxide layer on the surface of unpolished SUS 316 and SUS 316L spacers was estimated by
- 27 considering the decrease in the oxygen concentration and the increase in the Cr and Fe
- concentration (dotted line). As shown in Figure 4a and b, after approximately 15 s of sputtering
- 29 the concentration of oxygen decreases to almost half of the initial concentration for SUS 316,
- while the concentration of oxygen on the surface of SUS 316L reaches its half value after almost
- 23 s of sputtering. [48] The data clearly shows that the oxygen, Cr and Fe concentrations reach a
- 32 plateau at different levels for the two materials. SUS 316L maintains a significantly higher
- 33 oxygen concentration than SUS 316, which can be attributed to the pronounced diffusion of

1 oxygen into the surface of SUS 316L. This results in a self-healing effect (recombination of the

oxygen with the metal) for SUS 316L that enhances its relative corrosion resistance.

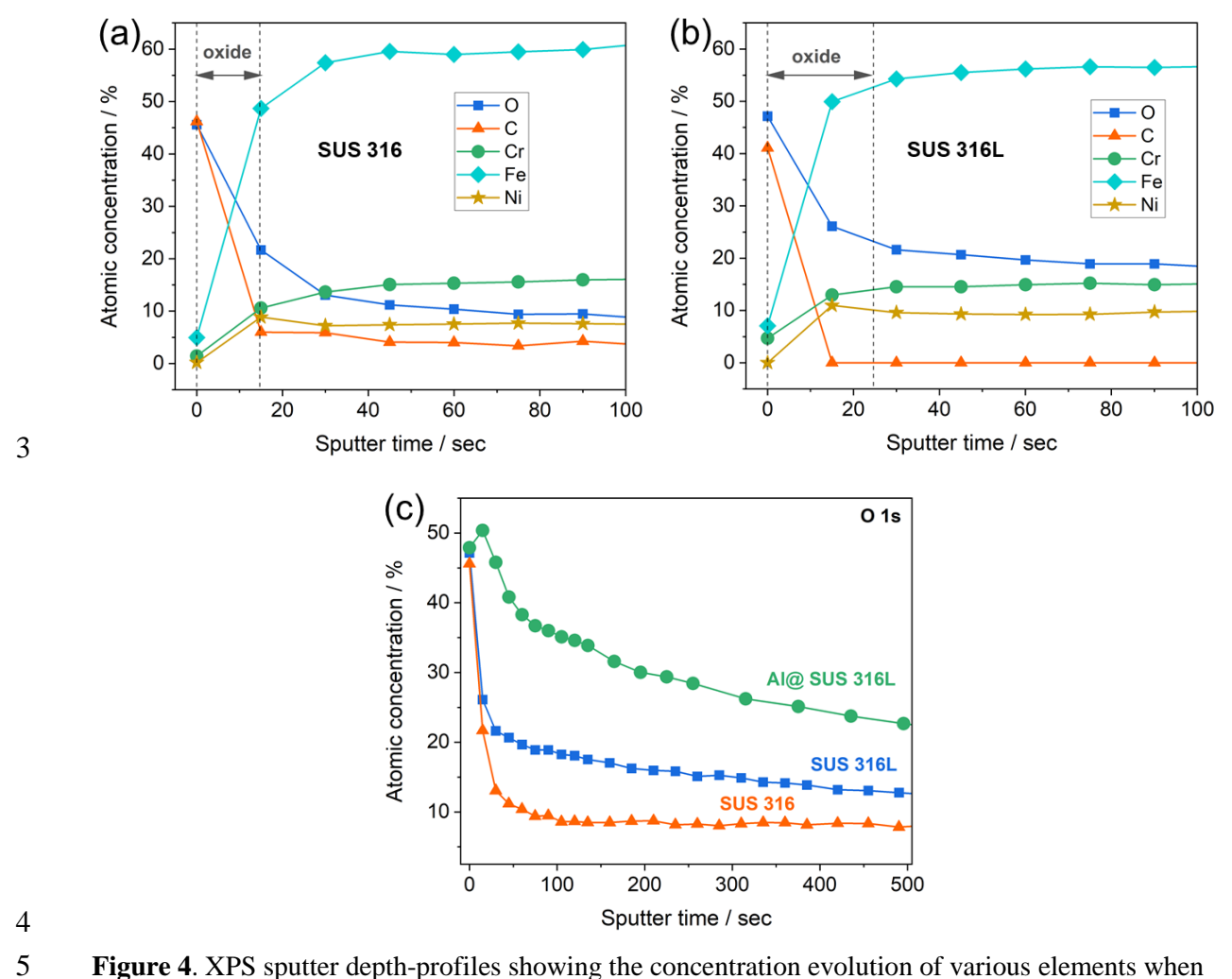


Figure 4. XPS sputter depth-profiles showing the concentration evolution of various elements when sputtering the top 36 nm (100 s of sputtering) of a) SUS 316 and b) SUS 316L pristine spacer surfaces. c) Comparison of the O 1s concentration between SUS 316 (spacer), SUS 316L (spacer) and Al_{CVD}@SUS 316L (case) CR 2032 coin-cell parts measured during 500 s of depth profile sputtering.

The surface and bulk concentration of Cr and Fe is also different for the two stainless-steel grades, with higher Cr concentration in SUS 316L and higher Fe concentration in SUS 316. This implies the higher dissolution resistance with reduced pitting formation for SUS 316L, which is in accordance with the results of the LSV measurements. It is known that SUS 316 and SUS 316L grades are mostly made of austenite phase, while the interaction of the Cl⁻-ions with the surface oxide layer was shown to differ depending on the stainless-steel phase. In case of austenite phase, the adsorption of Cl⁻-ions occurs preferentially at the austenite phase|oxide layer interface, thus inducing the destabilization of the Cr₂O₃ passivation film. [49,50] Figure 4c shows evolution of oxygen concentration (O 1s) with sputter time for the various materials. Based on the results of the electrochemical measurements, an Al₂O₃-coated SUS 316L coin cell part, denoted as Al_{CVD}@SUS 316L, was also used in these experiments. The comparison of the

- O 1s evolution indicates that the surface of SUS 316L behaves differently SUS 316 material.
- 2 Specifically, it appears to be more prone to re-passivation, resulting in higher dissolution
- 3 resistance.

9

10

11

12

13

14

15

16

17

18

19

20

21

22

23

24

25

26

27

28

- 4 Based on the presented results, the role of the native oxide layer at the surface of SUS 316 and
- 5 SUS 316L spacers in coin cells cycled with LiFSI-based electrolyte formulations, can be
- 6 summarized by the schematic representation in **Figure 5**.

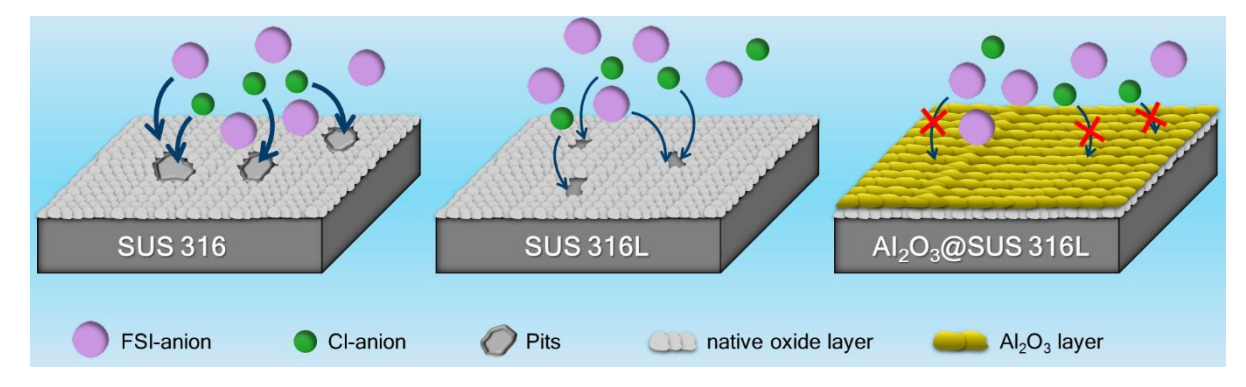


Figure 5. Schematic representation of the mechanism of pitting dissolution on different SUS substrates in LiFSI-based electrolytes. The right panel highlights the beneficial effect of combining material characteristics and Al_2O_3 coating, as it is the case of Al_{CVD} @SUS 316L.

The schematic in Figure 5 indicates that the presence of Cl⁻-ion impurities in the LiFSI salt results in a break-down of the stainless-steel native oxide layer and formation of pits while the FSI anions propagate the growth of these pits. Such mechanism in electrolyte formulations containing blended salts (LiPF₆ and LiFSI) is different depending on the stainless-steel grade, although pit formation was observed with both stainless-steel grades. Larger pits are formed on the surface of the SUS 316 compared to SUS 316L, despite the fact that both stainless-steels (SUS 316 and SUS 316L) contain a similar amount of Fe and Cr, with the only difference in the C content. These two metals and their corresponding oxides behave differently at high voltage in electrolyte formulations containing only LiPF₆ salt with the surface of Cr metal being able to be passivated to a CrF₃ film in contrary to Fe and its Fe₂O₃ oxide where no such passivation by LiPF₆ could be provided.^[51] This could also indicate that with LiPF₆ and LiFSI blended salts, the Fe dissolution is mostly responsible for the stainless-steel dissolution induced by both the Cl⁻ and FSI⁻ anions in the two stainless-steel grades. Thus, the different behavior of the stainless-steel dissolution at higher voltage in SUS 316L compared to SUS 316 can be related to either the slightly thicker Cr₂O₃ oxide layer present on SUS 316L or its ability to faster repassivate itself (Figure 4). Furthermore, the results presented in Figure 1 and Figure 2, where the stainless-steel dissolution kinetic, though the amount of current evolved at higher voltages, support the schematic representation in Figure 5. With an additional Al₂O₃ coating on

- the SUS 316L case, the use of an Al-spacer, and the presence of LiPF₆ co-salt, the stainless-
- 2 steel dissolution process in LiFSI-based electrolytes can be successfully avoided.

- 4 2.5. Electrochemical performance using an optimized CR 2032 design
- 5 In order to overcome the SUS dissolution, Al₂O₃ coated SUS 316L case and a 1 mm Al-disk
- 6 spacer were used to prepare the electrochemical cells. Using the Al₂O₃ and Al-disk spacer and
- 7 SUS 316L cell components for the cell assembly, the electrochemical performances of the
- 8 LMR $\parallel\mu$ -Si cells were evaluated using the electrolytes with various concentrations of LiPF₆ and
- 9 LiFSI conducting salts. Due to the stainless-steel dissolution resistance shown by the SUS 316L
- steel as well as the Al₂O₃ coating, all cells could be galvanostatically cycled to 4.65 V during
- the activation cycle, and between 4.4 V and 2.5 V for the subsequent cycles, independent of the
- 12 LiFSI electrolyte concentration. The results of these investigations are presented in **Figure 6**.

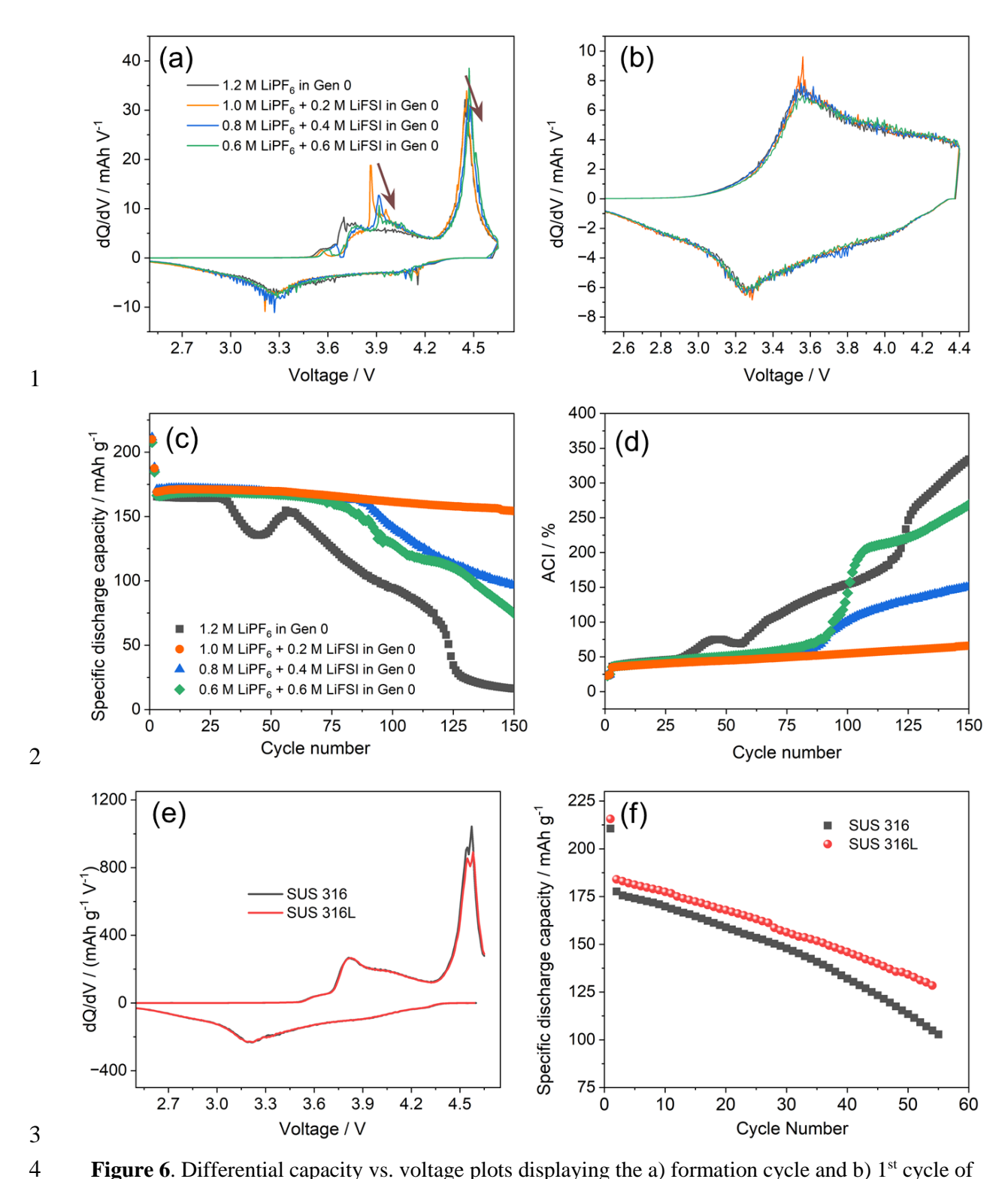


Figure 6. Differential capacity vs. voltage plots displaying the a) formation cycle and b) 1st cycle of the LMR||μ-Si cells with the LiFSI-based electrolytes and 1.2 M LiPF₆ in Gen 0. c) Galvanostatic cycling performance of LMR||μ-Si cells with Al_{CVD}@SUS 316L coin cells casing and Al spacer and LiFSI and 1.2 M LiPF₆ in Gen 0 electrolytes. d) The accumulated Coulombic inefficiency (ACI) of the LMR||μ-Si cells. e) Comparison between the dQ/dV plot of the LMR||μ-Si cells with SUS 316 and SUS 316L within the formation cycle. f) Galvanostatic cycling performance at C/10 and 20°C of LMR||μ-Si cells with SUS 316 and SUS 316L assembled with 4 M LiFSI + 0.6 M LiPF₆ in Gen 0.

Figure 6a,b presents the dQ/dV plots recorded during the formation and 1^{st} cycle of the cells assembled with the LMR cathode, μ -Si anode with Al spacer and Al_{CVD}@SUS 316L coin cell

1 casing using the LiFSI based electrolytes. For comparison purposes, data for the LiFSI-free electrolyte, i.e. 1.2 M LiPF₆ in Gen 0, is included. No noteworthy differences of the redox 2 3 reactions during the formation cycle were observed for the various electrolytes, with the 4 exception of small shifts (with increasing amount of LiFSI) to more positive voltages for the 5 oxidation process at ~ 3.9 V and the Li₂MnO₃ activation process at 4.47 V. Figure 6c presents 6 the specific discharge capacity calculated based on the cathode active material (N/P 2.58:1) for 7 the LMR||µ-Si cells investigated with the electrolyte solutions using a C-rate of 0.1 C during the formation and 1st cycle, while the following cycles were carried out at 0.33 C-rate. The cells 8 9 using 1.0 M LiPF₆ + 0.2 M LiFSI in Gen 0 show a stable galvanostatic cycling performance with a reversible specific capacity of 161.5 mAh g⁻¹ (CE₁₀₀th ~99.8%) after 100 cycles. In 10 contrast, lower specific capacity values of 142 mAh g⁻¹ (CE₁₀₀th ~98.2%) and 128 mAh g⁻¹ 11 12 $(CE_{100}^{th} \sim 84.4\%)$ were delivered for 0.8 M LiPF₆ + 0.4 M LiFSI in Gen 0 and 0.6 M LiPF₆ + 13 0.6 M LiFSI in Gen 0, respectively. However, the electrolyte formulation without LiFSI showed deteriorating galvanostatic cycling performance (94.6 mAh g⁻¹ and a CE ~99.8% after 14 15 100 cycles) that led to an increased accumulation of the coulombic inefficiency (ACI) as is 16 shown in Figure 6d. Such enhanced performance for the LiFSI containing electrolytes can be 17 attributed to an improved electrode electrolyte interface stability. 18 The tradeoff between the use of LiFSI and stainless-steel cells was achieved with high 19 concentration electrolytes (HCE) and localized high concentration electrolytes (LHCE) able to 20 overcome the side reactions encountered in LIBs, but also to improve the electrochemical performances of a specific battery chemistry. [52,53] An electrolyte formulation with LiFSI based 21 on 0.6 M LiPF₆ + 0.6 M LiFSI in Gen 0 was prepared by increasing the concentration of LiFSI 22 23 to 4 M. The LMR ||μ-Si cells were assembled with such HCE electrolytes, using SUS 316 and 24 SUS 316L coin cell parts without Al-coating. The electrochemical investigations for these cells 25 are presented in Figure 6e, f and the results indicate that using HCE with LiFSI it is possible to 26 cycle the LMR||μ-Si cells with a C-rate of C/10 with using common coin cell parts. There is no 27 effect of the LiFSI concentration and type of stainless-steel on the redox reactions (Figure 6e), 28 however, it is clear that the cells assembled with SUS 316L perform slightly better than the 29 cells assembled with SUS 316 coin cell parts (Figure 6f). The results indicate that using a 30 concentration of 4 M LiFSI in the Gen 0-based electrolyte, the stainless-steel dissolution 31 observed with LiFSI and SUS 316 and SUS 316L coin cell parts can be suppressed. To further 32 investigate whether the HCE electrolyte is able to suppress the stainless-steel dissolution, LSV 33 measurements were carried out with the HCE electrolyte (Figure S7) and SEM images were 34 recorded after these measurements (Figure S8). Although the evolved current density was very

small in comparison with the results presented in Figure 1, the SEM images revealed that the formation of pits is occurring. However, with an HCE electrolyte and with a sweep rate of 50 μV s⁻¹, a similar size of the stainless-steel dissolution pits as for the low concentration electrolyte is obtained when a sweep rate of 250 µV s⁻¹ as used. The lower specific current observed for the highly concentrated LiFSI electrolyte suggests that the kinetic of the stainlesssteel dissolution is further suppressed, [52] while the increase of viscosity implies also that less solvent molecules are able to dissolve the stainless-steel dissolution products. [33] The changes in the electrolyte's characteristic properties with increasing LiFSI concentration are responsible for the poor electrochemical performance. In summary, electrochemical measurements combined with morphological investigations provided insights into the stainless-steel dissolution in LiFSI-based electrolyte formulations. The suggested mechanism highlights an effect of the stainless-steel composition on the dissolution process, a process that was previously mentioned also by other authors. [33,38] The results also underline the importance of salt impurities for the electrochemical performance, therefore, more development work regarding salt purification methods should be done, as the purity plays an important role for the overall cell performance.^[37] It is imperative that particular attention be accorded to the side reactions (i.e. stainless-steel dissolution) taking place in laboratory cells when LiFSI-based electrolytes are utilized. Conversely, when considering a practical application, the cost and relevant physicochemical and electrochemical properties of the electrolyte formulations are of significant interest.

3. Conclusion

The electrochemical performance of LMR|| μ -Si cells containing electrolyte formulations with LiFSI and LiPF₆ co-salts varied strongly depending on the composition of the stainless-steel cell components and additional coatings. The stainless-steel dissolution process with the formation and growth of pits seems to be dependent on various parameters: LiFSI concentration in the electrolyte, scan rate (LSV) if the cell voltage is scanned to voltage above 4.2 V, composition of the SUS cell components and possibly the amount of Cl⁻ impurity in the LiFSI conducting salt. Independent of the LiFSI concentration, the stainless-steel dissolution process made it impossible to operate cells containing LMR cathode and μ -Si anode using exclusively SUS 316 parts. In contrast, using SUS 316L coin cell parts with low concentrations of LiFSI (e.g. 1.0 M LiPF₆ + 0.2 M LiFSI in Gen 0) in the electrolyte, electrochemical performance during the initial cycles are mainly dominated by the redox reactions occurring at the two electrodes with the stainless-steel dissolution being less evident. However, after a certain

number of cycles, stainless-steel dissolution again became predominant over the electrochemical redox reactions at the two electrodes. Furthermore, LSV measurement showed that the oxidative stainless-steel dissolution produced a lower current intensity on SUS 316L stainless-steel grade, implying that this material possesses a higher stainless-steel dissolution resistance than SUS 316 that is more common in CR 2032 parts. Furthermore, HCE electrolytes were able to further suppress stainless-steel dissolution, but were not completely able to overcome this unwanted reaction. Based on these results, a mechanism was derived showing that although the SUS 316L has a higher resistance towards stainless-steel dissolution, this material is not able to completely avoid the formation and growth of pits on its own. By using Al coated SUS 316L coin cell parts, the stainless-steel dissolution process was overcome, offering the possibility to investigate the electrochemical performance of LMR||μ-Si cells using LiFSI-based electrolytes.

4. Experimental details

Formulation of electrolytes: Considered electrolytes were formulated by mixing battery grade lithium bis(fluorosulfonyl)imide (LiFSI, Arkema) and lithium hexafluorophosphate (LiPF₆, E-Lyte Innovations) in various molar ratios (LiPF₆ to LiFSI molar ratio = 2:1; 1:1 and 1:2). The solvent mixture of EC/EMC 3/7 (by volume), denoted though out the text for simplicity as Gen 0, contained also 3 wt.% of fluoroethylene carbonate (FEC), 1 wt.% of vinylene carbonate (VC), 1 wt.% of 1,3,2-dioxathiolane 2,2-dioxide (DTD), 0.5 wt.% of lithium tetrafluoroborate (LiBF₄) and 0.5 wt.% of 1,3-propane sultone (PS) as electrolyte additives. The total Li⁺-ion concentration in all considered electrolyte formulations was kept to 1.2 M. A high concentration electrolyte (HCE) was prepared by dissolving the amount of LiFSI to the Gen 0 solvent mixture in order to obtain a concentration of LiFSI of 4 M.

Ionic conductivity measurement: The overall ionic conductivity of the electrolyte formulations was determined by means of electrochemical impedance spectroscopy (EIS), using the module of the HTE system as previously reported. The conductivity cells and the modules were filled and sealed inside the Glovebox (MBraun, H₂O and O₂ level lower than 0.1 ppm). The modules were placed inside a climatic chamber (Memmert TTC256) that allows the measurements to be carried out in a wide temperature range, in this case from -30 °C to 60 °C using 10 °C increments. Impedance measurements were measured in a frequency range of 20 kHz to 50 Hz and were conducted on a Metrohm Autolab potentiostat/galvanostat equipped with 8×12-channel multiplexer. Fitting of the impedance was carried out using a standard electrical circuit. The

electrodes used for these measurements were reported elsewhere^[54] and the cell constants were

determined using a standardized 0.01 M KCl solution (VWR) at 20 °C.

2

5

6

7

9

10

11

12

4 Polishing process for SUS spacers: Prior to the electrochemical measurements, the SUS 316

and SUS 316L spacers (1 mm thickness) were polished to mirror quality using a polishing

machine Tegramin-25 (Struers). Special inhouse insets were prepared by 3D-printing using the

masked direct light projection method on a Elegoo Mars 2 Pro using a Phrozen Aqua 4k resin.

8 These insets allowed a tight fit mounting of the 1 mm spacers in the polishing machine holder.

The mirror quality was obtained by polishing the 1 mm spacer for at least 10 min using three

diamond polishing suspensions with a grain size of 9 µm, 6 µm and 1 µm (DP-Suspension P,

Struers) on polishing cloths (MD-Sat, MD-Dac and MD-Nap, Struers). After each polishing

step, the SUS spacers were cleaned inside the ultrasonic bath for 5 min using deionized water.

13

17

18

19

20

21

22

23

24

26

27

28

29

Constant current measurements: Galvanostatic cycling performance of the LMR||μ-Si cells were evaluated in coin cells CR 2032, where the negative part (cap) with the 1.4 mm spring and

16 0.5 mm thick spacer (15 mm diameter) were always made out of SUS 316 stainless-steel

(Gelon). The case and the 1 mm spacer for the positive electrode were made of SUS 316

(Gelon), SUS 316L (Hohsen, Japan) and Al@SUS 316L (Hohsen, Japan) grade steel. In all coin

cells, 35 µL of the electrolyte was added dropwise to the Celgard 2500 separator (16 mm

diameter). The galvanostatic cycling was carried out in the voltage range of 4.4 V to 2.5 V at a

C-rate of 0.33 C with the exception of the initial two cycles. The first charge process,

representing the LMR activation, was carried out until a cut-off voltage value of 4.65 V using

a C-rate of 0.1 C (discharge to 2.5 V at 0.1 C) while in the second cycle the charge voltage cut-

off was limited to 4.4 V using a C-rate of 0.1 C (discharge to 2.5 V at 0.1 C). The positive Li-

25 Mn-rich (LMR, active material loading 5.24 mAh cm⁻¹, 14 mm diameter) and the micro-

crystalline Si electrodes (μ-Si, 11.9 mAh cm⁻¹, 15 mm diameter) were kindly provided by LG

ES. The current for the C-rate was calculated based on the cathode active material loading on

each cathode disk, since in all cases the N/P ratio was 2.27:1, thus cathode limited. All

galvanostatic measurements were carried out using a battery testing device Maccor 4000 series

30 (Maccor).

31

32 Potentiodynamic anodic polarization: Linear sweep voltammetry (LSV) experiments were

carried out in 2-electrode SUS||Li cells using a VMP-3 multichannel potentiostat (BioLogic).

34 The voltage was scanned with various scan rates from OCV to 5 V. For the determination of

- the pitting potential, a 3-electrode CR2032 coin cells was used: a lithium reference electrode
- 2 (Li metal on insulated Ni strip) was inserted between the two Celgard 2500 separator sheets
- 3 separating the SUS-based working electrode (WE) and the Li-metal counter electrode (CE,
- 4 15 mm diameter, 150 μm). [55] In this particular case, the potential of the WE (SUS-based spacer)
- 5 was scanned from open circuit potential (OCP) to 5 V vs. Li/Li⁺. Different scan rates were used
- and these are mentioned in the text. All electrochemical measurements were carried out at 20 °C,
- 7 while all cells were assembled inside an Ar-filled glove box (MBraun) with oxygen and
- 8 moisture values lower than 0.1 ppm.

- 10 Structural characterization of materials: The morphological changes of the Li electrode and
- cell materials (i.e. coin cell spacer) were investigated by means of scanning electron microscope
- 12 (SEM, Carl-Zeiss CrossBeam 550) using an acceleration voltage of 3 kV and a working
- distance (WD) of 5 mm. The elemental composition of the materials surface was determined
- using the energy-dispersive X-ray spectroscopy (EDX) by employing an Ultim Extreme
- detector (Oxford Instruments) and the AZtec software (Oxford Instruments, version 4.4.7495.1).
- 16 X-ray photoelectron spectroscopy (XPS) investigations carried out at nanoAnalytics GmbH
- using an "K-Alpha" spectrometer (Thermo VG Scientific) equipped with an Al-Kα source
- 18 (1486.6 eV). The sputter depth profiling was carried out using a MAGICS ion source (Thermo
- 19 Scientific), using monoatomic Ar ion beam. CasaXPS 2.3.24 software was used for data
- 20 evaluation.

21

22

23

Acknowledgements

- 24 The authors thank LG Energy Solution for the financial funding of this work through the
- 25 Frontier Research Laboratory (FRL) program.

26

2728

References

- 29 [1] M. Winter, B. Barnett, K. Xu, Chemical Reviews 2018, 118, 11433.
- 30 [2] F. Wu, S. Fang, M. Kuenzel, A. Mullaliu, J.-K. Kim, X. Gao, T. Diemant, G.-T. Kim, S. Passerini, *Joule* **2021**, *5*, 2177.
- 32 [3] R. Schmuch, R. Wagner, G. Hörpel, T. Placke, M. Winter, *Nature Energy* **2018**, *3*, 267.
- 33 [4] K. Xu, Chemical Reviews **2014**, 114, 11503.
- 34 [5] T. Famprikis, P. Canepa, J. A. Dawson, M. S. Islam, C. Masquelier, *Nature Materials* **2019**, *18*, 1278.
- 36 [6] Y. Shao, L. Knijff, F. M. Dietrich, K. Hermansson, C. Zhang, *Batteries & Supercaps* **2021**, *4*, 585.

- 1 [7] S. Jeschke, P. Johansson, *Batteries & Supercaps* **2021**, *4*, 1156.
- 2 [8] H. El-Bousiydy, T. Lombardo, E. N. Primo, M. Duquesnoy, M. Morcrette, P. Johansson, P. Simon, A. Grimaud, A. A. Franco, *Batteries & Supercaps* **2021**, *4*, 758.
- 4 [9] T. Lombardo, M. Duquesnoy, H. El-Bouysidy, F. Årén, A. Gallo-Bueno, P. B.
- Jørgensen, A. Bhowmik, A. Demortière, E. Ayerbe, F. Alcaide et al., *Chemical Reviews* **2022**, *122*, 10899.
- 7 [10] A. Narayanan Krishnamoorthy, C. Wölke, D. Diddens, M. Maiti, Y. Mabrouk, P. Yan, M. Grünebaum, M. Winter, A. Heuer, I. Cekic-Laskovic, *Chem. Methods* **2022**, 2, e202200008.
- 10 [11] F. Rahmanian, M. Vogler, C. Wölke, P. Yan, S. Fuchs, M. Winter, I. Cekic-Laskovic, H. S. Stein, *Scientific Data* **2023**, *10*, 43.
- 12 [12] Y.-Y. Wang, X.-Q. Zhang, M.-Y. Zhou, J.-Q. Huang, *Nano Research Energy* **2023**, 2, e9120046.
- 14 [13] A. Kolesnikov, M. Kolek, J. F. Dohmann, F. Horsthemke, M. Börner, P. Bieker, M. Winter, M. C. Stan, *Adv. Energy Mater.* **2020**, *10*, 2000017.
- [14] J. F. Dohmann, F. Horsthemke, V. Küpers, S. Bloch, Y. Preibisch, A. Kolesnikov, M.
 Kolek, M. C. Stan, M. Winter, P. Bieker, *Adv. Energy Mater.* 2021, *11*, 2101021.
- [15] D. Lin, Y. Liu, Y. Li, Y. Li, A. Pei, J. Xie, W. Huang, Y. Cui, *Nature Chemistry* **2019**,
 11, 382.
- [16] D. T. Boyle, W. Huang, H. Wang, Y. Li, H. Chen, Z. Yu, W. Zhang, Z. Bao, Y. Cui,
 Nature Energy 2021, 6, 487.
- 22 [17] B. Kwon, J. Lee, H. Kim, D.-M. Kim, K. Park, S. Jo, K. T. Lee, *J. Mater. Chem. A* **2021**, 9, 24993.
- 24 [18] X. Wang, E. Yasukawa, S. Mori, *Electrochimica Acta* **2000**, *45*, 2677.
- 25 [19] S. Zhang, T. Jow, *Journal of Power Sources* **2002**, *109*, 458.
- [20] E. Krämer, T. Schedlbauer, B. Hoffmann, L. Terborg, S. Nowak, H. J. Gores, S.
 Passerini, M. Winter, *Journal of The Electrochemical Society* 2013, *160*, A356.
- [21] C. Behling, J. Lüchtefeld, S. J. Wachs, K. J. Mayrhofer, B. B. Berkes, *Electrochimica Acta* 2024, 473, 143480.
- 30 [22] E. Krämer, S. Passerini, M. Winter, ECS Electrochemistry Letters 2012, 1, C9.
- 31 [23] P. Meister, X. Qi, R. Kloepsch, E. Krämer, B. Streipert, M. Winter, T. Placke, 32 *ChemSusChem* **2017**, *10*, 804.
- 33 [24] R.-S. Kühnel, M. Lübke, M. Winter, S. Passerini, A. Balducci, *Journal of Power Sources* **2012**, *214*, 178.
- 35 [25] S. Theivaprakasam, G. Girard, P. Howlett, M. Forsyth, S. Mitra, D. MacFarlane, *npj*36 *Materials Degradation* **2018**, 2, 13.
- 37 [26] X. Zhang, X. Dong, X. Yue, J. Gao, Z. Shi, J. Liu, Y. Dong, Y. Chen, M. Fang, H. Yu et al., *Adv. Energy Mater.* **2024**, *n/a*, 2403588.
- 39 [27] A. Heckmann, M. Krott, B. Streipert, S. Uhlenbruck, M. Winter, T. Placke, 40 *ChemPhysChem* **2017**, *18*, 156.
- [28] X. Li, S. Deng, M. N. Banis, K. Doyle-Davis, D. Zhang, T. Zhang, J. Yang, R.
 Divigalpitiya, F. Brandys, R. Li et al., ACS Applied Materials & Interfaces 2019, 11,

43 32826.

- 44 [29] K. N. Shitaw, M. A. Weret, Y. Nikodimos, T. M. Tekaligne, S.-K. Jiang, C.-J. Huang, 45 B.-H. Lin, S.-H. Wu, W.-N. Su, B. J. Hwang, *Materials Today Energy* **2024**, *39*, 101461.
- 47 [30] H. Luo, H. Su, C. Dong, K. Xiao, X. Li, Construction and Building Materials **2015**, 96, 502.
- 49 [31] S. Grugeon, S. Laruelle, L. Dupont, F. Chevallier, P. L. Taberna, P. Simon, L. Gireaud, S. Lascaud, E. Vidal, B. Yrieix et al., *Chemistry of Materials* **2005**, *17*, 5041.

- 1 [32] L. Dupont, S. Laruelle, S. Grugeon, C. Dickinson, W. Zhou, J.-M. Tarascon, *Journal of Power Sources* **2008**, *175*, 502.
- 3 [33] C. Luo, Y. Li, W. Sun, P. Xiao, S. Liu, D. Wang, C. Zheng, *Electrochimica Acta* **2022**, 419, 140353.
- 5 [34] X. Wu, Z. Du, *Electrochemistry Communications* **2021**, *129*, 107088.
- 6 [35] V. Sharova, A. Moretti, T. Diemant, A. Varzi, R. Behm, S. Passerini, *Journal of Power Sources* **2018**, *375*, 43.
- 8 [36] P. Bai, X. Ji, J. Zhang, W. Zhang, S. Hou, H. Su, M. Li, T. Deng, L. Cao, S. Liu et al., 9 *Angew. Chem. Int. Ed.* **2022**, *61*, e202202731.
- 10 [37] H.-B. Han, S.-S. Zhou, D.-J. Zhang, S.-W. Feng, L.-F. Li, K. Liu, W.-F. Feng, J. Nie, H. Li, X.-J. Huang et al., *Journal of Power Sources* **2011**, *196*, 3623.
- 12 [38] H.-H. Strehblow, *Materials and Corrosion* **1984**, *35*, 437.
- 13 [39] C.-O. Olsson, D. Landolt, *Electrochimica Acta* **2003**, *48*, 1093.
- 14 [40] V. S. Saji, ChemElectroChem **2023**, 10, e202300136.
- 15 [41] T. Evans, J. Olson, V. Bhat, S.-H. Lee, *Journal of Power Sources* **2014**, 269, 616.
- [42] J. Hirpara, V. Chawla, R. Chandra, *Journal of Materials Engineering and Performance* 2021, 30, 1895.
- 18 [43] X. Chen, W. Xu, J. Xiao, M. H. Engelhard, F. Ding, D. Mei, D. Hu, J. Zhang, J.-G. Zhang, *Journal of Power Sources* **2012**, *213*, 160.
- [44] X. Wang, S. Li, W. Zhang, D. Wang, Z. Shen, J. Zheng, H. L. Zhuang, Y. He, Y. Lu,
 Nano Energy 2021, 89, 106353.
- 22 [45] H. J. Kim, N. Voronina, H. Yashiro, S.-T. Myung, *ACS Applied Materials & Interfaces* 23 **2020**, *12*, 42723.
- [46] X. Zhao, Z. Zhao-Karger, M. Fichtner, X. Shen, *Angewandte Chemie (International ed. in English)* 2020, 59, 5902.
- 26 [47] H. J. Kim, H. Yashiro, H. Kim, S. Lee, S.-T. Myung, J. Mater. Chem. A 2019, 7, 26250.
- 27 [48] H. B. Lee, J. Chen, S. Meng, C. Jang, S. H. Park, Q. Xiao, H. J. Lee, K.-H. Na, *Journal of Nuclear Materials* **2021**, *556*, 153193.
- [49] B. Zhang, X. X. Wei, B. Wu, J. Wang, X. H. Shao, L. X. Yang, S. J. Zheng, Y. T. Zhou,
 Q. Q. Jin, E. E. Oguzie et al., *Corrosion Science* 2019, 154, 123.
- 31 [50] H. Xu, L. Wang, D. Sun, H. Yu, Applied Surface Science 2015, 351, 367.
- [51] S.-T. Myung, Y. Sasaki, S. Sakurada, Y.-K. Sun, H. Yashiro, *Electrochimica Acta* **2009**,
 55, 288.
- 34 [52] Q. Liu, T. L. Dzwiniel, K. Z. Pupek, Z. Zhang, *Journal of The Electrochemical Society* **2019**, *166*, A3959-A3964.
- 36 [53] Y. Yang, Z. Yang, Z. Li, J. Wang, X. He, H. Zhao, *Adv. Energy Mater.* **2023**, *13*, 2302068.
- 38 [54] Hans-Dieter Wiemhöfer, Mariano Grünebaum, Martin Manuel Hiller, WO2014139494A1.

43

40 [55] D. Juarez-Robles, C.-F. Chen, Y. Barsukov, P. P. Mukherjee, *Journal of The Electrochemical Society* **2017**, *164*, A837.